Journal of Energy Chemistry 124 (2027) 968–976

Contents lists available at ScienceDirect

Journal of Energy Chemistry

journal homepage: www.elsevier.com/locate/jechem

http://www.journals.elsevier.com/journal-of-energy-chemistry/

Heterostructured catalytic interfaces enable uniform lithium atom diffusion toward dendrite-free Li metal batteries

Yongfeng Jia [a], Yingying Zhang [a], Lei Ji [a,b,*], Quan Zhuang [a], Zhao Li [c], Yongzheng Zhang [d], Kaier Shen [e], Jinghai Liu [a,*], Jian Wang [f,g,*]

[a] Inner Mongolia Engineering Research Centre of Lithium-Sulfur Battery Energy Storage, Inner Mongolia Key Laboratory of Solid State Chemistry for Battery, College of Chemistry and Materials Science, Inner Mongolia Minzu University, Tongliao 028000, Inner Mongolia, China
[b] Peking University Ordos Research Institute of Energy, Ordos 017000, Inner Mongolia, China
[c] Department of Materials, Imperial College London, London SW7 2AZ, United Kingdom
[d] School of Textile & Clothing, Nantong University, Nantong 226019, Jiangsu, China
[e] Beijing Key Laboratory for Theory and Technology of Advanced Battery Materials, School of Materials Science and Engineering, Peking University, Beijing 100871, China
[f] Helmholtz Institute Ulm (HIU), Ulm D89081, Germany
[g] Karlsruhe Institute of Technology (KIT), Karlsruhe D76021, Germany

ARTICLE INFO

Article history:
Received 9 July 2026
Revised 2 September 2026
Accepted 9 September 2026
Available online 23 September 2026

Keywords:
Lithium metal anodes
Heterostructured catalytic interfaces
TiN-NbC nanofibers
Li-atom diffusion
Dendrite-free deposition

ABSTRACT

Lithium metal anodes are regarded as promising anode materials owing to the ultrahigh theoretical specific capacity and the lowest electrochemical potential, making them a prime candidate for next-generation high-energy–density batteries. However, uncontrolled dendrite growth and electrode pulverization severely hinder their practical deployments, which are mainly attributed to sluggish Li ion/atom diffusion. Herein, the local heterostructure-improved electrical field strategy of constructing a flexible TiN-NbC nanofiber membrane (TN-CNFM) has been initially proposed, establishing a stable catalytic interphase to modulate Li atom migration kinetics. Density functional theory (DFT) calculations and experimental characterizations reveal that the TiN-NbC heterojunction interphase significantly reduces the diffusion energy barrier of Li atom, promotes lateral Li atom redistribution and uniform Li nucleation/growth, effectively suppressing dendrite formation. As a result, the optimal Li anode with TN-CNFM interphase exhibits a low overpotential and an ultralong cycle lifespan exceeding 1600 h at 5 mA cm^{-2}. The full cells paired with $LiNi_{0.8}Co_{0.1}Mn_{0.1}O_2$ (NCM811) cathodes stabilize the capacity retention of 81.3% at 0.5C after 400 cycles and reach the robust capacity of 150.7 mA h g^{-1} at 5C. This work presents a catalytic interface strategy for precisely controlling lithium deposition dynamics and enhancing anode stability.

© 2026 The Authors. Published by Published by Elsevier B.V. and Science Press on behalf of Science Press and Dalian Institute of Chemical Physics, Chinese Academy of Sciences. This is an open access article under the CC BY license (http://creativecommons.org/licenses/by/4.0/).

1. Introduction

Lithium metal is regarded as the promising anode material owing to its ultrahigh theoretical specific capacity (3860 mA h g^{-1}) and lowest redox potential (−3.04 V vs. SHE), offering the potential to boost the energy density of next-generation batteries [1–6]. However, the practical development of lithium metal anodes (LMAs) remains hindered by uneven Li deposition, dendritic growth, and unstable solid electrolyte interphase (SEI), which collectively induce severe volumetric fluctuations, electrolyte depletion, and low Coulombic efficiency, particularly under high current densities [2,4,6–14] or extremely tough conditions. Conventional strategies to suppress dendrite growth focus on regulating Li nucleation/growth behavior at the lithium/solid-electrolyte interface [6,9]. While substantial progress has been made, LMAs still suffer from interfacial instability and unstable Li ion flux, primarily due to their "hostless" nature, particularly under high current densities [15,16]. Carbonaceous scaffolds have emerged as promising materials for LMA carriers and current collectors, owing to their high conductivity and large surface area, which help reduce local current density [11,17–21]. Additionally, robust porous or hollow carbon frameworks mitigate volume expansion

* Corresponding authors.
E-mail addresses: jilei@ordos.pku.edu.cn (L. Ji), jhliu2015@imun.edu.cn (J. Liu), jian.wang@kit.edu, wangjian2014@sinano.ac.cn (J. Wang).

https://doi.org/10.1016/j.jechem.2026.09.027
2095-4956/© 2026 The Authors. Published by Published by Elsevier B.V. and Science Press on behalf of Science Press and Dalian Institute of Chemical Physics, Chinese Academy of Sciences.
This is an open access article under the CC BY license (http://creativecommons.org/licenses/by/4.0/).
Open access funding enabled and organized by Projekt DEAL.

during lithium deposition [10,22–25]. However, the lithiophobic nature of carbon materials leads to high nucleation barriers, impeding controlled lithium growth [4,12,26–29]. The accumulated interfacial stresses during cycling exacerbate this issue, as lithium atoms preferentially deposit at sites with higher ionic conductivity, generating mechanical stress beneath the SEI. This stress is relieved through lithium deformation, which in turn triggers dendritic growth.

Surface modification engineering including heteroatom doping, lithiophilic site introduction, and functional group modification aims to tailor the surface chemistry of carbon carriers [3,22,25,30–35]. Nevertheless, the mechanistic details and control over the morphology and composition of these approaches remain poorly understood. As established, lithium deposition behavior is strongly influenced by current density and Li^+/atom diffusion rates. Fractal dendrites accumulate localized radial stresses through inhomogeneous and uncontrolled deposition [22,23,36]. To address dendrite-related challenges, regulating deposition behavior at electrode/electrolyte interfaces while ensuring structural stability is crucial [24–29,37–40]. In our previous work, the single atom catalyst decorated carbon interphase had demonstrated that regulating the interfacial kinetics of Li ions could help to delocalize the atom distribution for smooth plating [15,41–43]. Therefore, an ideal host or interfacial regulator for lithium metal anodes should combine mechanical robustness, chemical stability, regulated electronic/ionic transport, stable electrode/electrolyte interfaces, and low inactive mass.

Herein, we report a flexible TiN-NbC carbon nanofiber membrane (TN-CNFM) as a stable catalytic interphase to modulate Li migration kinetics. The conductive carbon nanofiber network provides a lightweight and flexible scaffold to reduce local current density and accommodate repeated Li plating/stripping, whereas the embedded TiN-NbC heterostructures serve as catalytic sites to couple Li nucleation regulation with accelerated Li-atom surface diffusion. The TiN-NbC catalyst nanoparticles, partially embedded within the conductive carbon nanofibers with accessible surface/near-surface sites, provides active sites to promote lateral diffusion of Li and lower the diffusion barrier. This enables uniform nucleation, smooth deposition morphology, and stabilized SEI formation. Benefiting from fast interfacial charge transport, Li-atom migration, and structural stability, the Li@TN-CNFM composite anode delivers stable Li plating/stripping for over 1600 h at 5 mA cm^{-2} with an areal capacity of 1 mA h cm^{-2}, high Coulombic efficiency in Li||Cu cells, and superior full-cell performance when paired with $LiNi_{0.8}Co_{0.1}Mn_{0.1}O_2$ cathodes, retaining 81.3% of its capacity after 400 cycles at 0.5C.

2. Results and discussion

To construct a diffusion-regulating catalytic interface, a flexible TN-CNFM was prepared by electrospinning and followed by high-temperature treatment, as illustrated in Fig. S1, with detailed synthetic procedures provided in the Supporting Information. Tetrabutyl titanate (TBOT) and niobium pentoxide (Nb_2O_5) were used as the Ti and Nb sources, respectively, while polyacrylonitrile (PAN) served simultaneously as the carbon source and fiber-forming matrix. Subsequent pyrolysis at 1000 °C yielded a self-supporting, mechanically flexible, and highly interwoven nanofiber membrane (Fig. S2). The TN-CNFM has a thickness of 40 μm and an areal loading of 1.0 mg cm^{-2} (Fig. S3). Such an interconnected conductive scaffold is favorable for reducing local current density and maintaining structural integrity during repeated Li plating/stripping (Fig. 1a).

The morphology and microstructure of the TN-CNFM were characterized by scanning electron microscopy (SEM) and transmission electron microscopy (TEM). As shown in Fig. 1(b), the TN-CNFM exhibits a continuous, randomly interwoven fibrous network with fiber diameters of approximately 100 ~ 300 nm. TEM further reveals that TiN and NbC nanoparticles are uniformly distributed within the carbon nanofiber, with some domains located at or near the fiber surface rather than being completely encapsulated by a continuous carbon shell (Fig. 1c). High-resolution TEM (HRTEM) shows clear lattice fringes with interplanar spacings of 0.245 and 0.223 nm (Fig. 1d), corresponding to the TiN (1 1 1) and NbC (2 0 0) planes, respectively. Both phases are indexed to cubic structures with the *Fm*-3 *m* space group, confirming the coexistence of crystalline TiN and NbC. Selected-area electron diffraction (SAED, Fig. 1e) further confirms the crystalline nature of TN-CNFM, displaying well-defined diffraction rings assignable to the TiN (1 1 1), (2 2 0), and (2 2 2) planes as well as the NbC (2 0 0) and (3 3 1) planes. Energy-dispersive X-ray spectroscopy (EDS) elemental mapping (Fig. 1f) reveals the homogeneous distribution of Ti, Nb, N, and C throughout the nanofibers.

The crystalline structure of the TN-CNFM was further examined by X-ray diffraction (XRD). The diffraction pattern exhibits characteristic reflections of both TiN and NbC phases (Fig. 2a). Specifically, the peaks at 36.6°, 42.5°, 62.0°, 74.3°, and 78.3° can be assigned to the (1 1 1), (2 0 0), (2 2 0), (3 1 1), and (2 2 2) planes of cubic TiN, respectively (JCPDS No. 38-1420). In addition, the reflections at 34.7°, 40.3°, 58.3°, 73.3°, and 87.1° correspond to the (1 1 1), (2 0 0), (2 2 0), (2 2 2), and (4 0 0) planes of cubic NbC, respectively (JCPDS No. 38-1364). The N_2 adsorption–desorption isotherm exhibits a distinct hysteresis loop, and the corresponding pore-size distribution confirms the mesoporous architecture of TN-CNFM (Fig. S4), which is beneficial for electrolyte penetration and interfacial Li^+ transport.

X-ray photoelectron spectroscopy (XPS) was conducted to probe the surface chemical states of TN-CNFM. In the Ti 2*p* spectrum (Fig. 2b), the spin–orbit doublets located at 455.6/461.4, 456.9/462.7, and 458.6/464.3 eV are assigned to Ti-N, Ti-N-O, and Ti-O species, respectively. The Ti-O component is mainly attributed to slight surface oxidation or adsorbed oxygen during air exposure. The Nb 3*d* spectrum (Fig. 2c) exhibits two sets of characteristic doublets at 204.4/206.3 and 207.5/210.5 eV, corresponding to Nb–C and Nb–O species, respectively, confirming carbide bonding with surface-oxidized Nb species. In the C 1*s* spectrum (Fig. S5a), the dominant peaks at 284.7 and 285.4 eV are assigned to sp^2- and sp^3-hybridized C–C bonds, respectively, while the weaker signals at 286.6 and 283.7 eV correspond to C–O–C and Nb–C bonds. The N 1*s* spectrum (Fig. S5b) is deconvoluted into four components at 396.1, 397.4, 399.0, and 401.2 eV, which are attributed to Ti-N-C, Ti-N, Ti-N-O, and N-O species, respectively. These nitride/carbide chemical states provide interfacial sites for regulating Li nucleation and diffusion.

The local coordination environments and electronic structures of Nb and Ti in TN-CNFM were investigated by X-ray absorption fine structure (XAFS) spectroscopy. The Nb *K*-edge XANES spectrum (Fig. 2d) shows that the absorption edge of TN-CNFM lies between those of Nb foil and NbO_2, indicating a subvalent $Nb^{\delta+}$ state associated with Nb–C bonding rather than metallic Nb^0. The Fourier transform of the extended X-ray absorption fine structure (FT-EXAFS) spectrum (Fig. 2e) exhibits a dominant peak at approximately 1.71 Å, attributable to first-shell Nb–C coordination, whereas metallic Nb–Nb and oxide-like Nb–O contributions are not dominant. Consistently, the WT-EXAFS contour plot (Fig. 2f) displays a main intensity maximum at approximately 4.5 $Å^{-1}$ in the Nb–C coordination region, confirming the NbC-like local environment (Fig. S6 and Table S1). The Ti *K*-edge XANES spectrum (Fig. 2g) shows that the absorption edge of TN-CNFM lies between those of Ti foil and TiO_2, indicating an average Ti valence state higher than metallic Ti^0 but lower than Ti^{4+} in TiO_2. This result is

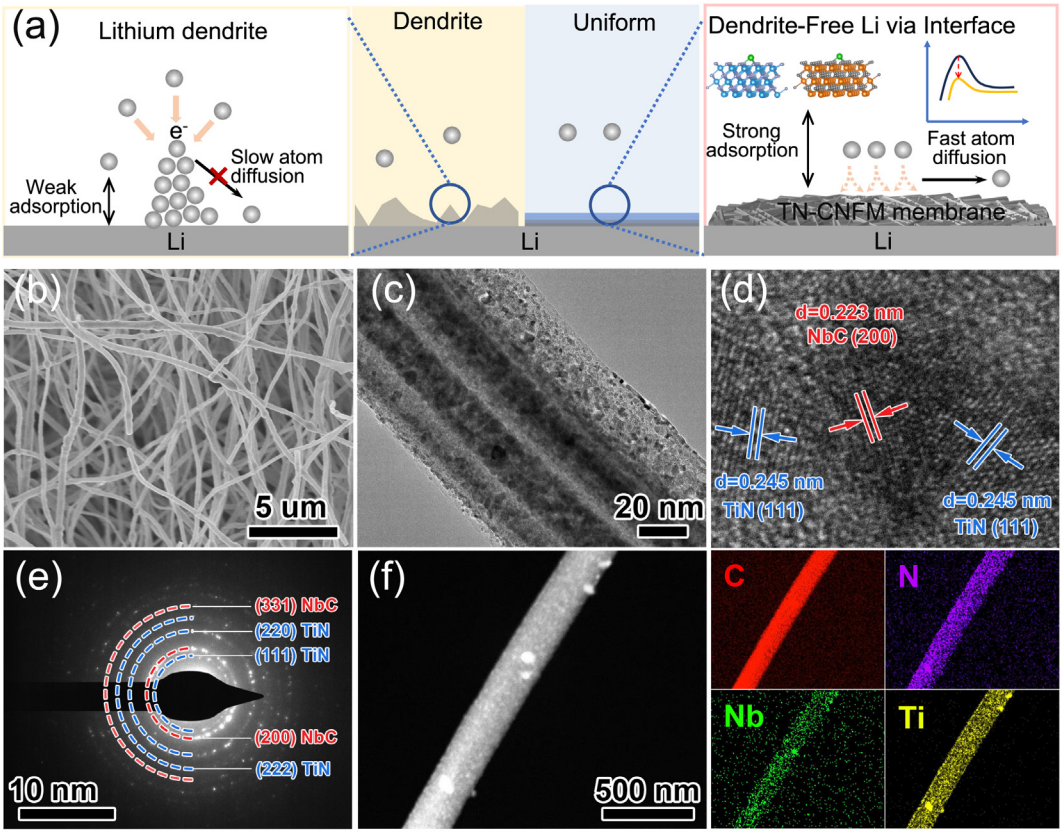


Fig. 1. Fabrication and structural characterization of the TiN-NbC heterostructure-embedded carbon nanofiber membrane (TN-CNFM). (a) Schematic illustration of Li electrodeposition on pristine Li metal and at the TN-CNFM-regulated interface. (b) SEM image. (c) TEM image. (d) HRTEM showing TiN and NbC lattice fringes. (e) SAED pattern. (f) HAADF-STEM image and corresponding elemental mappings of Ti, Nb, N, and C.

consistent with a TiN-dominated electronic structure, with minor contributions from Ti-O/Ti-O-N species. The FT-EXAFS spectrum of TN-CNFM exhibits a distinct Ti-(N/O) first-shell scattering contribution, accompanied by Ti-Ti second-shell scattering associated with the TiN-like framework, supporting the preservation of a TiN-like local coordination structure (Fig. 2h). The Ti-(N/O) assignment is adopted because Ti-N, Ti-O-N, and surface Ti-O scattering paths may overlap in the first-shell region, consistent with the slight surface oxidation/oxynitridation indicated by XPS. WT-EXAFS further supports that the local coordination environment of TN-CNFM is closer to TiN than to TiO_2 or metallic Ti (Fig. 2i). The TiN/NbC heterostructures embedded within and exposed on the conductive carbon nanofibers provide chemically active coordination environments, forming the structural basis for a catalytic interface that regulates Li-atom diffusion (Fig. S7 and Table S2).

To evaluate the Li plating/stripping behavior regulated by the TN-CNFM, a Li@TN-CNFM anode was prepared by pressing the TN-CNFM onto the Li metal surface, followed by assembling Li@TN-CNFM||Li@TN-CNFM symmetric cells. Galvanostatic cycling was performed at a fixed areal capacity of 1 mA h cm^{-2} under current densities ranging from 0.5 to 5.0 mA cm^{-2} (Fig. 3a). At 0.5 mA cm^{-2}, the Li@TN-CNFM||Li@TN-CNFM cell exhibits a flat voltage plateau with a low voltage hysteresis, indicating facilitated Li plating/stripping kinetics. When the current density increases to 1.0, 2.0, and 5.0 mA cm^{-2}, the voltage hysteresis remains as low as 24, 39, and 80 mV, respectively, corresponding to only 52%, 44%, and 38% of those of the pristine Li electrode (Fig. S8). These reduced polarization values demonstrate that TN-CNFM effectively redistributes Li^+ flux and lowers the kinetic barrier for interfacial Li deposition, thereby enabling stable Li plating/stripping under high-rate conditions. Electrochemical impedance spectroscopy (EIS) was further performed to probe the interfacial charge-transfer behavior of the Li-based cells (Fig. S9a, b). Compared with the pristine Li electrode, the Li@TN-CNFM electrode shows markedly decreased series resistance (R_S) and charge-transfer resistance (R_{ct}), suggesting reduced interfacial impedance and facilitated charge transfer at the electrode/electrolyte interface. Moreover, the comparable LSV responses of TN-CNFM and bare CC (Carbon Cloth) indicate that the exposed TiN-NbC heterointerfaces do not induce appreciable additional electrolyte decomposition within the investigated potential range (Fig. S10).

To evaluate the long-term Li plating/stripping stability, symmetric cells were tested under different current densities and areal capacities. The Li@TN-CNFM electrode delivers highly stable cycling for up to 4800 h, far exceeding that of the control cell, which fails after 1295 h (Fig. S11). At a fixed areal capacity of 1 mA h cm^{-2}, the Li@TN-CNFM symmetric cell maintains a stable voltage profile for over 1200 h, whereas pristine Li shows pronounced polarization fluctuations and fails after approximately 791 h (Fig. 3b), indicating severe interfacial degradation. The Li@TN-CNFM electrode also exhibits robust stability at high current densities. At 2 mA cm^{-2}, it maintains a low overpotential over 800 h (Fig. S12). Even at 5 mA cm^{-2}, stable cycling is sustained for over 1600 h with a low and steady overpotential (Fig. S13). These results demonstrate that the TN-CNFM interface effectively stabilizes Li deposition and suppresses dendrite-induced failure. As summarized in Fig. 3(c, d) and Table S3, the cycling stability of Li@TN-CNFM compares favorably with recently reported Li metal

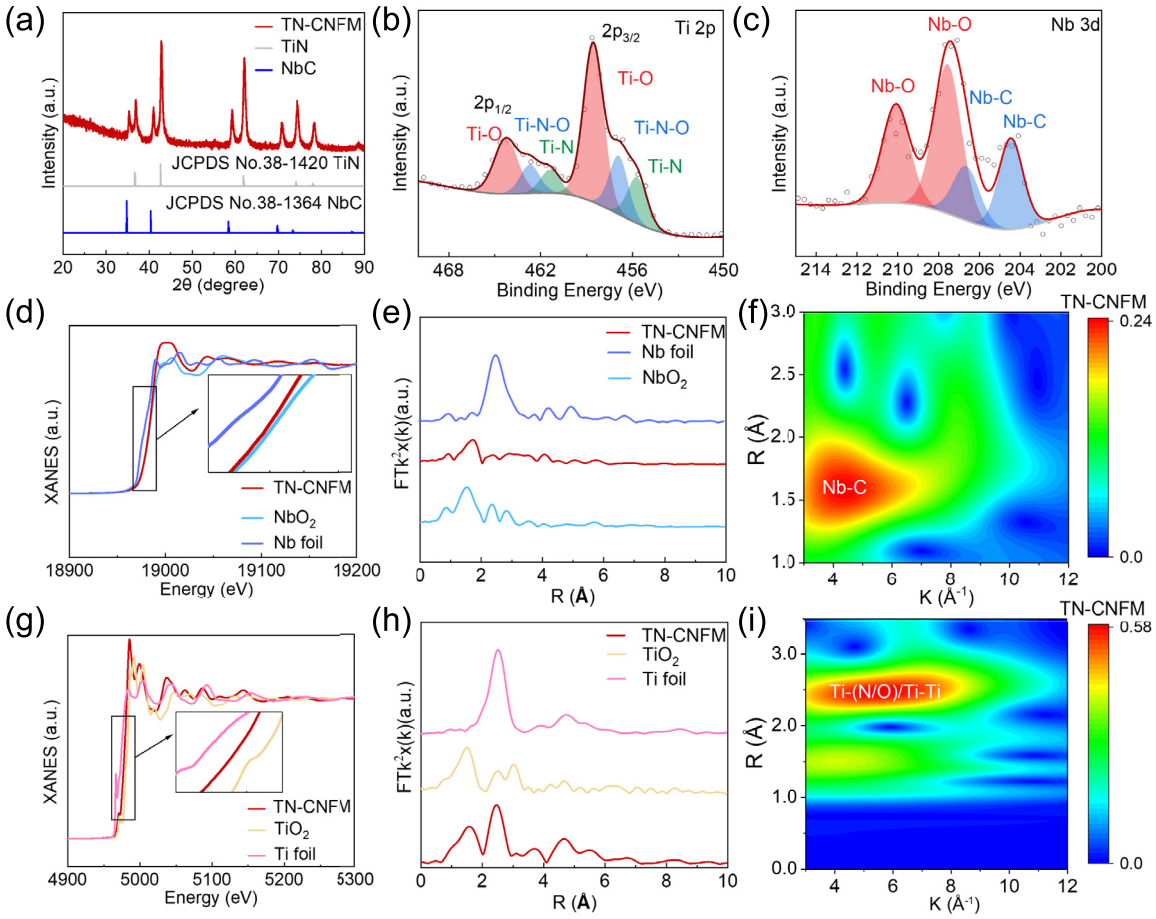


Fig. 2. Phase structure, surface chemistry, and local coordination environment of TN-CNFM. (a) XRD pattern. (b, c) High-resolution XPS spectra of Ti 2*p* and Nb 3*d*. (d, g) Normalized Nb and Ti *K*-edge XANES spectra, (e, h) k^3-weighted FT-EXAFS spectra at the Nb and Ti *K*-edges. (f, i) WT-EXAFS contour plots at the Nb and Ti *K*-edges.

anodes. The stable voltage response directly verifies that the TN-CNFM interface redistributes Li flux and promotes delocalized Li deposition, thereby enabling prolonged cycling stability.

To further evaluate the reversibility of Li plating/stripping, Coulombic efficiency (CE) was measured in Li||Cu asymmetric cells. The TN-CNFM-modified Cu electrode, denoted as Cu@TN-CNFM, exhibits a low Li nucleation overpotential of 32 mV, markedly lower than that of bare Cu (68 mV; Fig. 3e), indicating enhanced Li affinity and regulated nucleation behavior. At 0.5 mA cm^{-2}, Cu@TN-CNFM maintains a stable average CE of 98.85% over 120 cycles, whereas bare Cu shows pronounced CE fluctuations and premature failure (Fig. S14a), reflecting uncontrolled Li deposition. Even at higher current densities of 1 and 2 mA cm^{-2}, Cu@TN-CNFM delivers high average CEs of 98.80% and 98.02%, respectively (Fig. 3f and Fig. S14b). The improved reversibility is attributed to the TiN-NbC heterostructured catalytic interface, which lowers Li nucleation barriers, promotes Li atom surface diffusion, and favors planar Li deposition. Meanwhile, time-resolved EIS/DRT analysis further reveals that the initial sloped transient is mainly associated with the progressive establishment of the Li/TN-CNFM interface and coupled charge-transfer/nucleation dynamics, rather than continuous SEI thickening or increasing ion-transport resistance through the porous membrane (Fig. S15). These results confirm that TN-CNFM serves as a kinetically active and structurally stable diffusion modulator layer for homogenizing Li flux and suppressing localized Li accumulation.

To evaluate the effectiveness of TN-CNFM under a restricted Li inventory, 10 mA h cm^{-2} of Li was electrochemically deposited onto TN-CNFM to construct a limited-Li anode (10Li@TN-CNFM), with 10Li@Cu used as the control (Fig. S16). The 10Li@TN-CNFM|| 10Li@TN-CNFM cell maintained stable plating/stripping for 100 h at 5 mA cm^{-2} and 1 mA h cm^{-2} (Fig. S17b), while reversible Li deposition with an average Coulombic efficiency of 96.27% was maintained at 1 mA cm^{-2} (Fig. S17a). Moreover, the NCM811|| 10Li@TN-CNFM cell delivered 171.0 mA h g^{-1} initially and retained 92.9% after 100 cycles at 0.5C (Fig. S18). These results confirm the effectiveness of TN-CNFM under practically restricted Li inventory.

To evaluate the full-cell compatibility of the Li@TN-CNFM electrode, coin-type cells were assembled using Li@TN-CNFM as the anode and NCM811 as the cathode. As shown in Fig. 3(g), the Li@TN-CNFM-based full cell delivers a high specific capacity of 150 mA h g^{-1} at 5C, retaining 79.9% of the capacity obtained at 0.5C (188 mA h g^{-1}). This value is 1.64 times higher than that of the pristine Li-based cell at 5C (91.8 mA h g^{-1}). At 0.5C, the Li@TN-CNFM||NCM811 full cell retains 153 mA h g^{-1} after 400 cycles, outperforming the pristine Li||NCM811 cell with only 118 mA h g^{-1}, demonstrating the improved interfacial stability enabled by the TN-CNFM interface (Fig. 3h). At 2C, the Li@TN-CNFM-based cell maintains a reversible capacity of 163 mA h g^{-1}, further highlighting the enhanced rate capability afforded by the regulated Li-metal interface (Fig. S19). Moreover, the NCM811|| Li@TN-CNFM full cell with a high cathode loading of 10 mg cm^{-2} exhibits stable cycling performance at 0.5C, further demonstrating the feasibility of the TN-CNFM-protected Li anode under practically relevant cathode loadings (Fig. S20). In Li||$LiFePO_4$ cells, the pristine Li-based cell undergoes rapid capacity fading, whereas

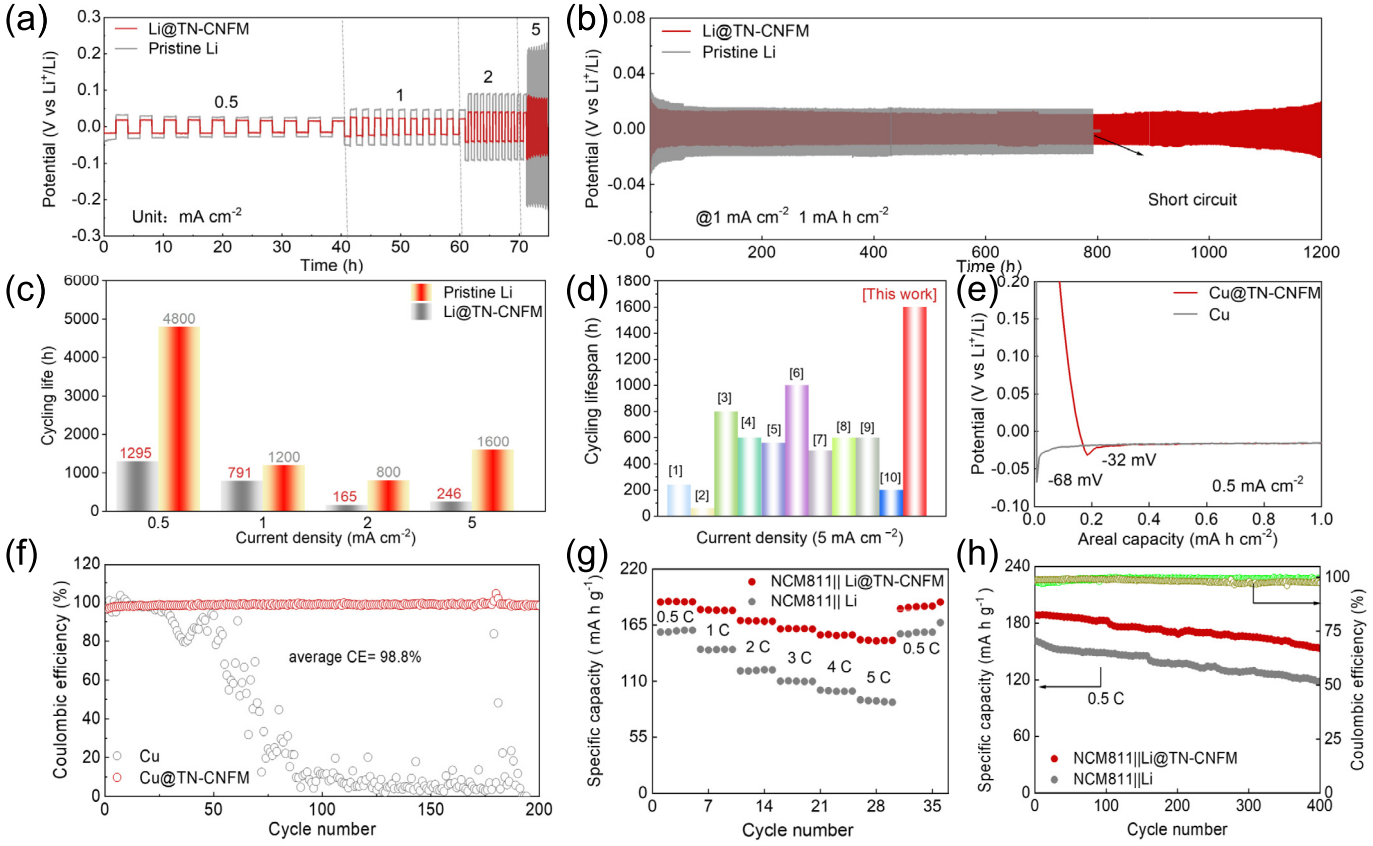


Fig. 3. Electrochemical performance of Li metal anodes regulated by the TN-CNFM interface. (a) Rate performance and voltage hysteresis of Li||Li and Li@TN-CNFM||Li@TN-CNFM symmetric cells. (b) Galvanostatic cycling stability. (c) Cycling lifetime comparison at different current densities. (d) Benchmark comparison with reported Li metal anodes. (e) Initial Li nucleation overpotentials on pristine Cu and Cu@TN-CNFM. (f) Coulombic efficiency of Li||Cu and Li||Cu@TN-CNFM cells measured in 1.0 M $LiPF_6$ in EC/DEC (1:1 by volume) at 1.0 mA cm^{-2} with a plating capacity of 1.0 mA h cm^{-2}. (g, h) Rate and cycling performance of Li||NCM811 full cells.

the Li@TN-CNFM-based cell delivers an initial capacity of 148 mA h g^{-1} at 1C and retains 141 mA h g^{-1} after 200 cycles, corresponding to a capacity retention of 95.1% (Fig. S21). In the Li-S battery system, when paired with a sulfur cathode, the Li@TN-CNFM-based cell achieves an initial discharge capacity of 1014 mA h g^{-1} at 1C and maintains 966 mA h g^{-1} after 200 cycles, corresponding to 95.3% retention (Fig. S22). These results indicate that TN-CNFM stabilizes Li metal anodes across different full-cell chemistries, underscoring its general role in regulating Li deposition kinetics. To further evaluate the applicability of TN-CNFM under a restricted Li inventory, an anode-free NCM811||Cu@TN-CNFM cell was assembled without any preloaded Li on the anode side. The cell delivered an initial capacity of 160 mA h g^{-1} at 0.5C and maintained a Coulombic efficiency of 97.4% over 50 cycles (Fig. S23), demonstrating the capability of TN-CNFM to regulate reversible Li deposition/stripping even without a pre-existing Li-metal reservoir.

To elucidate the Li deposition behavior regulated by the TN-CNFM interface, ex situ SEM characterization and density functional theory (DFT) calculations were conducted. After cycling, the Li@TN-CNFM electrode exhibits a dense and dendrite-free Li morphology, whereas pristine Li shows cracked, porous deposits with pronounced dendritic protrusions (Fig. S24). Even at a high areal capacity of 10 mA h cm^{-2}, TN-CNFM maintains an interconnected fibrous architecture without obvious Li aggregation (Figs. S25 and S26), indicating its ability to accommodate volume variation and guide dendrite-free plating morphology. The preserved upper fibrous network together with the dense underlying Li surface indicates that TN-CNFM acts primarily as an ion-permeable catalytic interfacial membrane, directing delocalized Li deposition predominantly toward the buried TN-CNFM/Li interface rather than being uniformly filled by metallic Li. Similar buried Li-growth behavior beneath ion-permeable artificial interfacial layers has also been experimentally observed in previous studies [3,44,45]. Depth-profiling XPS was further employed to elucidate the SEI chemistry on cycled Li electrodes. Compared with bare Li, the Li protected by TN-CNFM exhibits substantially suppressed carbonaceous species throughout the investigated depth, indicating mitigated solvent-derived parasitic reactions. Notably, the relative contribution of Li_2O in the O 1*s* spectra increases from the outer surface toward the inner SEI, accompanied by predominantly LiF fluorinated species (Fig. S27). In contrast, bare Li retains considerably higher carbon content together with pronounced high-binding-energy fluorinated species, indicative of a chemically heterogeneous interphase arising from continuous electrolyte decomposition (Fig. S28). These results suggest that TN-CNFM redirects the interfacial reaction toward a chemically reduced and inorganic-rich SEI, thereby stabilizing the Li/electrolyte interface during repeated plating/stripping (Fig. S29).

To further probe Li deposition at the interface, Li@TN-CNFM electrodes were plated to areal capacities of 1, 3, and 5 mA h cm^{-2}, followed by removal of the TN-CNFM layer for SEM observation of the underlying Li surface (Fig. 4a–c). At 1 mA h cm^{-2}, the exposed Li surface remains smooth and compact, without apparent dendritic protrusions. As the plating capacity increases to 3 and 5 mA h cm^{-2}, the underlying Li still maintains a dense and uniform morphology, with no visible mossy Li, needle-like dendrites, or localized Li accumulation. These results demonstrate that TN-

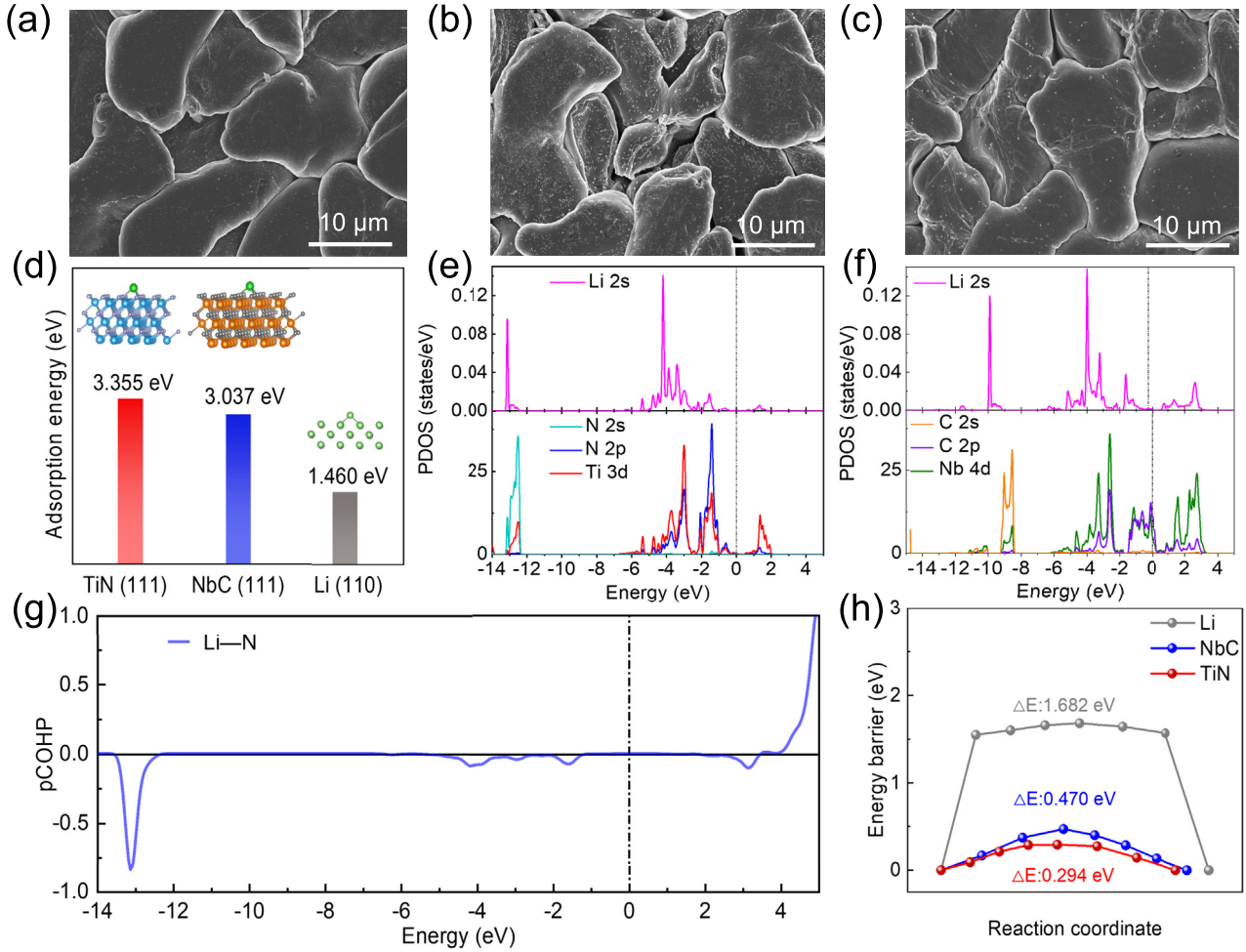


Fig. 4. Li deposition behavior and interfacial interaction at the Li/TN-CNFM interface. (a–c) SEM images of the exposed Li surface after removing the TN-CNFM layer at areal capacities of 1, 3, and 5 mA h cm^{-2}. (d) Calculated Li adsorption energies on different substrates. (e, f) PDOS of Li@TiN and Li@NbC. (g) COHP analysis of Li–N interactions. (h) Li-atom migration barriers on TiN(111), NbC(111), and Li (110) reference surface.

CNFM effectively regulates Li deposition by redistributing Li flux and facilitating lateral Li-atom diffusion, thereby suppressing vertical dendrite propagation and stabilizing the Li metal surface under high-capacity plating. In situ optical microscopy further reveals that TN-CNFM suppresses the amplification of preferential vertical growth sites and preserves a stable deposition front, consistent with enhanced lateral Li redistribution and delocalized deposition (Fig. S30).

To elucidate the role of the TN-CNFM interface in regulating Li nucleation and diffusion, DFT calculations were performed. On TiN (111), Li preferentially adsorbs at N-coordinated sites, while on NbC (111), Li mainly interacts with C-coordinated sites, giving rise to strong Li binding energies of 3.355 and 3.037 eV, respectively (Fig. 4d). These adsorption capability are markedly higher than that on the pristine Li(110) surface (1.460 eV), indicating that the TiN/NbC interface provides favorable lithiophilic sites for stabilizing Li atoms and lowering the Li nucleation barrier. The projected density of states (PDOS) reveals pronounced orbital hybridization between Li 2*s* and N 2*p*/C 2*p* states (Fig. 4e, f), supporting strong interfacial chemical interactions. Crystal orbital Hamilton population (COHP) analysis further confirms the robust Li–N and Li–C bonding, as evidenced by occupied bonding states with negligible antibonding contributions near the Fermi level (Fig. 4g and Fig. S31). The calculated migration barriers on TiN (111) and NbC (111) are 0.294 and 0.470 eV, respectively, markedly lower than that on metallic Li (1.682 eV; Fig. 4h). In particular, the low barrier on TiN (111) suggests that TiN-rich interfacial sites provide kinetically favorable pathways for Li atom surface diffusion.

To directly resolve the heterointerface-specific Li interaction, an explicit TiN(111)/NbC(111) model was further constructed (Fig. 5a). Pronounced charge redistribution is localized around the TiN-NbC phase boundary, and Bader analysis indicates a net interfacial charge transfer of approximately 4.06 e^- from NbC toward TiN (Fig. 5b). Consistently, the markedly different work functions of TiN (7.37 eV) and NbC (4.05 eV), together with the intermediate value of the coupled TiN-NbC system (6.26 eV), evidence substantial electronic reconstruction upon interfacial contact (Fig. 5c). The corresponding planar-averaged electrostatic-potential profile exhibits a pronounced potential variation across the TiN-NbC interfacial region, further corroborating the formation of an interfacial potential gradient associated with charge redistribution (Fig. S32). Li binding at representative local environments across the heterointerface reaches 4.392, 4.081, and 3.967 eV, respectively (Fig. 5d), demonstrating strong but spatially differentiated Li affinity near the phase boundary. Two representative Li-migration pathways were subsequently evaluated by CI-NEB (Fig. 5e, f). Path 1 exhibits a low migration barrier of approximately 0.31 eV, whereas Path 2 involves a metastable intermediate with a comparably low initial migration barrier, indicating that the TiN-

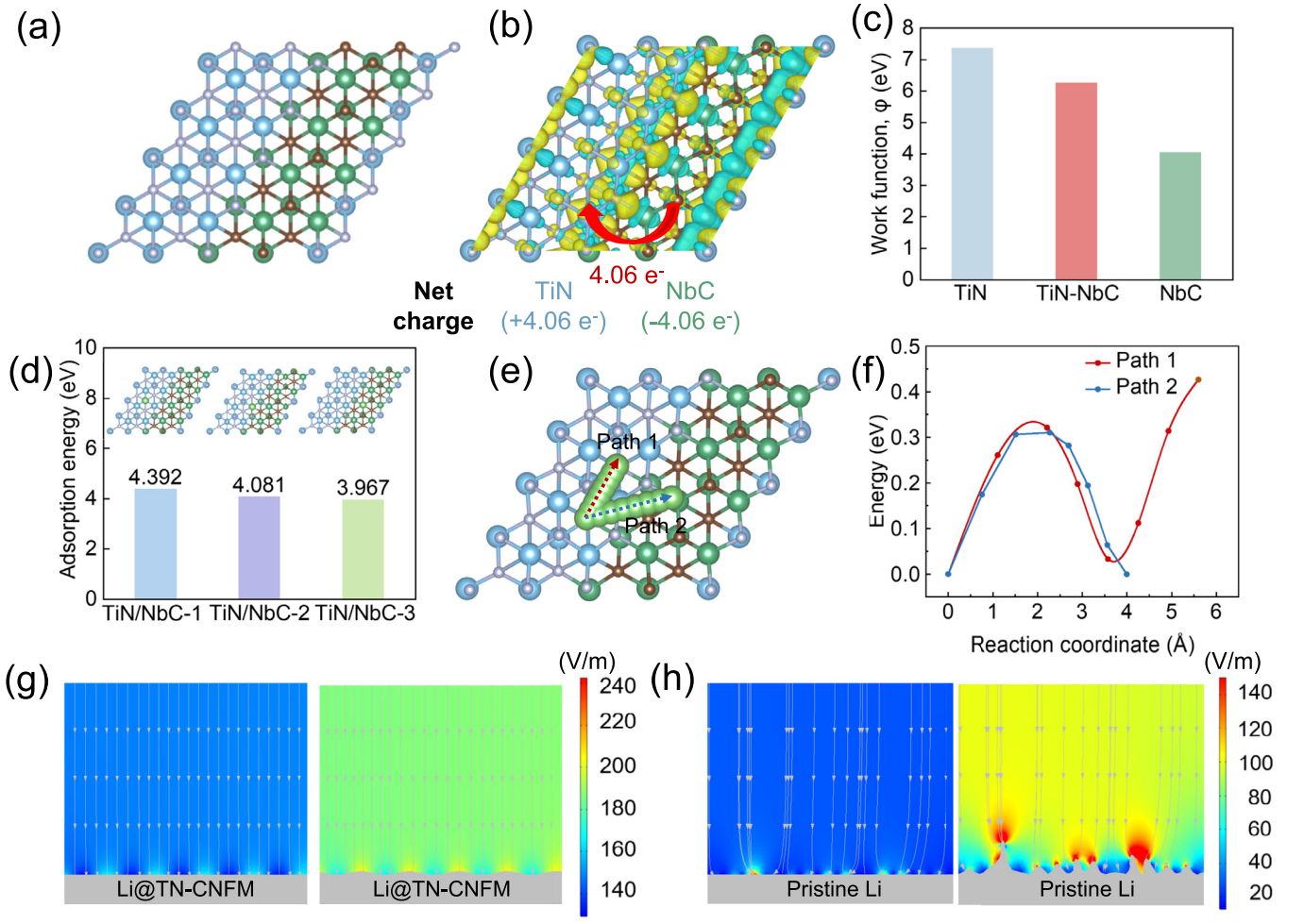


Fig. 5. Interfacial electronic reconstruction and Li-interaction kinetics at the TiN-NbC heterointerface. (a) Optimized atomic structure of the TiN(111)/NbC(111) heterointerface. (b) Charge-density-difference distribution and corresponding Bader charge transfer across the TiN-NbC phase boundary; yellow and cyan isosurfaces denote electron accumulation and depletion, respectively. (c) Calculated work functions of TiN(111), TiN-NbC, and NbC(111). (d) Representative Li adsorption configurations at different local environments of the TiN-NbC heterointerface, with corresponding Li binding energies of 4.392, 4.081, and 3.967 eV, respectively. (e) Representative Li atom migration pathways at the TiN-NbC heterointerface. (f) Corresponding CI-NEB energy profiles for Path 1 and Path 2, respectively. (g, h) COMSOL-simulated electric-field distributions at the Li@TN-CNFM/electrolyte and pristine Li/electrolyte interfaces at the initial state and after 90 s of Li deposition, respectively.

NbC interfacial region provides kinetically accessible pathways for Li atom redistribution. These results support an adsorption-diffusion coupling picture in which interfacial electronic reconstruction establishes favorable Li-binding environments while retaining low-barrier surface migration, consistent with the kinetic-activator mechanism proposed for delocalized Li deposition.

Finite-element simulations further reveal that TN-CNFM homogenizes the interfacial electric-field distribution and suppresses tip-induced field concentration, thereby evening the Li^+ flux; together with the reduced Li-atom migration barrier at the TiN-NbC heterointerface, this promotes lateral Li redistribution rather than localized vertical growth (Fig. 5g, h). The uniform Li deposition therefore arises from the coupled effects of the porous scaffold in homogenizing Li^+ flux and reducing local current density, together with TiN-NbC mediated nucleation and kinetically favorable Li atom surface redistribution, rather than from lateral Li diffusion alone. These results reveal an adsorption-diffusion coupling mechanism: TiN/NbC domains first stabilize Li atoms through Li binding energy and then act as kinetic activators to propel surface spreading and lateral redistribution. Consequently, the TiN-NbC heterostructured interface promotes uniform Li nucleation/growth and suppresses localized Li accumulation, enabling dendrite-free delocalized deposition.

3. Conclusions

In summary, we designed a flexible TiN-NbC heterostructure-embedded carbon nanofiber membrane (TN-CNFM) to construct a catalytic interphase for stabilizing lithium metal anodes. The embedded TiN-NbC heterostructured domains provide abundant lithiophilic/catalytic sites, which enhance Li affinity, lower Li-atom migration barriers, and promote lateral Li-atom redistribution without any dendrite formation. As a result, the Li@TN-CNFM anode delivers stable Li plating/stripping with low polarization, prolonged cycling stability, and improved Coulombic efficiency. Moreover, Li@TN-CNFM-based full cells paired with NCM811, $LiFePO_4$, and sulfur cathodes exhibit enhanced rate capability and cycling stability,

demonstrating applicability of this interfacial regulation strategy. This work provides a heterostructured catalytic-interface strategy for regulating Li deposition kinetics and advancing dendrite-free lithium metal batteries.

Experimental section

Experimental details can be found in the Supporting Information.

CRediT authorship contribution statement

Yongfeng Jia: Data curation. **Yingying Zhang:** Methodology, Investigation. **Lei Ji:** Writing – original draft, Project administration. **Quan Zhuang:** Software, Methodology, Investigation. **Zhao Li:** Software, Methodology, Investigation. **Yongzheng Zhang:** Methodology, Investigation. **Kaier Shen:** Methodology, Investigation. **Jinghai Liu:** Writing – review & editing, Supervision, Funding acquisition, Conceptualization. **Jian Wang:** Writing – review & editing, Supervision, Conceptualization.

Declaration of competing interest

The authors declare that they have no known competing financial interests or personal relationships that could have appeared to influence the work reported in this paper.

Acknowledgment

Dr. Jian Wang thanks the fellowship supported by the Alexander von Humboldt Foundation. This work was supported by the National Natural Science Foundation of China (22242003 and 22361035), the Opening funding from Engineering Research Center of Li-S battery storage (Inner Mongolia Minzu University) (MDK2025071), the Inner Mongolia Grassland Talents-Young Leading Talent Program (KYCYYC23002), the Natural Science Foundation of Inner Mongolia of China (2025JQ008, 2024QN02013, and 2026QC0118), and the Fundamental Research Funds for University of Inner Mongolia (GXKY26Z069). Additional support was provided by the Program for Innovative Research Team in Universities of Inner Mongolia Autonomous Region (NMGIRT2417) and the Fund for Supporting the Reform and Development of Local Universities (Discipline Construction).

Appendix A. Supplementary material

Supplementary data to this article can be found online at https://doi.org/10.1016/j.jechem.2026.09.027.

References

[1] C. Niu, D. Liu, J.A. Lochala, C.S. Anderson, X. Cao, M.E. Gross, W. Xu, J.-G. Zhang, M.S. Whittingham, J. Xiao, J. Liu, Nat. Energy 6 (2021) 723–732.
[2] S. Ko, T. Obukata, T. Shimada, N. Takenaka, M. Nakayama, A. Yamada, Y. Yamada, Nat. Energy 7 (2022) 1217–1224.
[3] Z. Huang, J.-C. Lai, S.-L. Liao, Z. Yu, Y. Chen, W. Yu, H. Gong, X. Gao, Y. Yang, J. Qin, C. Yi, Z. Bao, Nat. Energy 8 (2023) 577–585.
[4] H. Wan, Z. Wang, S. Liu, B. Zhang, X. He, W. Zhang, C. Wang, Nat. Energy 8 (2023) 473–481.
[5] H. Ji, J. Xiang, Y. Li, M. Zheng, L. Yuan, Y. Liao, L. Du, Z. Li, Z. Xie, K. Huang, X. Lin, Z. Xie, Y. Shen, M. Chen, T. Li, G. Feng, Y. Sun, L. Qie, H. Li, F. Zhang, R. Guo, X. Feng, W. Chen, X. Ai, J. Lu, Y. Huang, Nature 643 (2025) 1255–1262.
[6] S. Zhang, R. Li, N. Hu, T. Deng, S. Weng, Z. Wu, D. Lu, H. Zhang, J. Zhang, X. Wang, L. Chen, L. Fan, X. Fan, Nat. Commun. 13 (2022) 5431.
[7] G.M. Hobold, C. Wang, K. Steinberg, Y. Li, B.M. Gallant, Nat. Energy 9 (2024) 580–591.
[8] Z. Zhang, Y. Li, R. Xu, W. Zhou, Y. Li, S.T. Oyakhire, Y. Wu, J. Xu, H. Wang, Z. Yu, D.T. Boyle, W. Huang, Y. Ye, H. Chen, J. Wan, Z. Bao, W. Chiu, Y. Cui, Science 375 (2022) 66–70.
[9] S.T. Oyakhire, W. Zhang, A. Shin, R. Xu, D.T. Boyle, Z. Yu, Y. Ye, Y. Yang, J.A. Raiford, W. Huang, J.R. Schneider, Y. Cui, S.F. Bent, Nat. Commun. 13 (2022) 3986.
[10] J. Pokharel, A. Cresce, B. Pant, M.Y. Yang, A. Gurung, W. He, A. Baniya, B.S. Lamsal, Z. Yang, S. Gent, X. Xian, Y. Cao, W.A. Goddard III, K. Xu, Y. Zhou, Nat. Commun. 15 (2024) 3085.
[11] Q. Chen, B. Gao, Z. Yang, Y. Li, Q. Zhai, Y. Jia, Q. Zhang, X. Gu, J. Zuo, L. Wang, T. Wang, P. Zhai, C. Yang, Y. Gong, Nat. Commun. 15 (2024) 10045.
[12] M.S. Diallo, T. Shi, Y. Zhang, X. Peng, I. Shozib, Y. Wang, L.J. Miara, M.C. Scott, Q. H. Tu, G. Ceder, Nat. Commun. 15 (2024) 858.
[13] Y. Liang, F. Liu, J. Ren, X. Wang, H. Wang, J. Song, L. Feng, R. Wang, J. Energy Chem. 111 (2025) 316–327.
[14] P. Liu, T. Li, Y. Xiao, J. You, B. Zhang, Y. Liu, W. Wang, Y. Li, J. Energy Chem. 113 (2026) 217–227.
[15] J. Wang, B. Tang, J. Wu, J. Zhang, Z. Cao, H. Li, Y. Miao, H. Li, F. Wu, F. Liu, D. Wang, Y. Zhang, Q. Xiao, H. Lin, M. Fichtner, Sci. Adv. 12 (2026) eaef9111.
[16] J. Zhang, F. Liu, R. He, Q. Guan, N. Tian, J. Wu, Z. Cao, S. Yin, Y. Zhang, L. Jia, X. Li, C. You, H. Liu, M. Liu, Y. Miao, H. Lin, J. Wang, Adv. Mater. 37 (2025) e10894.
[17] T.-T. Lv, J. Liu, L.-J. He, H. Yuan, T.-Q. Yuan, J. Energy Chem. 98 (2024) 414–421.
[18] M.R. Shaik, Y. Park, Y.-K. Jung, W.B. Im, J. Energy Chem. 97 (2024) 120–127.
[19] Y. Gao, F. Qiao, N. Li, J. You, Y. Yang, J. Wang, C. Shen, T. Jin, X. Li, K. Xie, J. Energy Chem. 79 (2023) 390–397.
[20] J. Wang, Y. Wang, X. Lu, J. Qian, C. Yang, I. Manke, H. Song, J. Liao, S. Wang, R. Chen, Adv. Mater. 36 (2024) 2308257.
[21] S. Kim, I. Heo, J.H. Kang, M.S. Kang, J. Lee, H.S. Kim, D.-H. Lim, S.B. Cho, W.C. Yoo, J. Energy Chem. 113 (2026) 113–125.
[22] Z. Wu, C. Wang, Z. Hui, H. Liu, S. Wang, S. Yu, X. Xing, J. Holoubek, Q. Miao, H.L. Xin, P. Liu, Nat. Energy 8 (2023) 340–350.
[23] X. Yuan, B. Liu, M. Mecklenburg, Y. Li, Nature 620 (2023) 86–91.
[24] Z.-X. Wang, Y. Lu, C.-Z. Zhao, W.-Z. Huang, X.-Y. Huang, W.-J. Kong, L.-X. Li, Z.-Y. Wang, H. Yuan, J.-Q. Huang, Q. Zhang, Joule 8 (2024) 2794–2810.
[25] W. Zhai, B. Yuan, Y. Fan, Y. Zhang, X. Zhang, Y. Ma, W. Liu, Y. Yu, J. Am. Chem. Soc. 144 (2022) 4124–4132.
[26] T. Wang, B. Chen, Y. Liu, Z. Song, Z. Wang, Y. Chen, Q. Yu, J. Wen, Y. Dai, Q. Kang, F. Pei, R. Xu, W. Luo, Y. Huang, Science 388 (2025) 311–316.
[27] H. Gao, X. Ai, H. Wang, W. Li, P. Wei, Y. Cheng, S. Gui, H. Yang, Y. Yang, M.-S. Wang, Nat. Commun. 13 (2022) 5050.
[28] X.-B. Cheng, C. Yan, X. Chen, C. Guan, J.-Q. Huang, H.-J. Peng, R. Zhang, S.-T. Yang, Q. Zhang, Chem 2 (2017) 258–270.
[29] Y. Zhang, R. Qiao, Q. Nie, P. Zhao, Y. Li, Y. Hong, S. Chen, C. Li, B. Sun, H. Fan, J. Deng, J. Xie, F. Liu, J. Song, Nat. Commun. 15 (2024) 4454.
[30] J. Chen, X. Deng, X. Jia, Y. Gao, H. Chen, Z. Lin, S. Ding, J. Am. Chem. Soc. 146 (2024) 30836–30847.
[31] A.J. Sanchez, N.P. Dasgupta, J. Am. Chem. Soc. 146 (2024) 4282–4300.
[32] Q. Wang, C. Zhao, S. Wang, J. Wang, F. Wu, P. Ombrini, S. Ganapathy, S. Eustace, X. Bai, B. Li, M. Armand, D. Aurbach, M. Wagemaker, J. Am. Chem. Soc. 147 (2025) 9365–9377.
[33] P. Yu, H. Zhang, F. Hussain, J. Luo, W. Tang, J. Lei, L. Gao, D. Butenko, C. Wang, J. Zhu, W. Yin, H. Zhang, S. Han, R. Zou, W. Chen, Y. Zhao, W. Xia, X. Sun, J. Am. Chem. Soc. 146 (2024) 12681–12690.
[34] Q. Kang, Y. Li, Z. Zhuang, H. Yang, L. Luo, J. Xu, J. Wang, Q. Guan, H. Zhu, Y. Zuo, D. Wang, F. Pei, L. Ma, J. Zhao, P. Li, Y. Lin, Y. Liu, K. Shi, H. Li, Y. Zhu, J. Chen, F. Liu, G. Wu, J. Yang, P. Jiang, X. Huang, Adv. Mater. 36 (2024) 2308799.
[35] L. Rong, Y. Han, H. Yao, G. Liu, C. Zhang, X. Wang, T. Mei, J. Energy Chem. 105 (2025) 407–417.
[36] J. Wang, J. Zhang, S. Duan, L. Jia, Q. Xiao, H. Liu, H. Hu, S. Cheng, Z. Zhang, L. Li, W. Duan, Y. Zhang, H. Lin, Nano Lett. 22 (2022) 8008–8017.
[37] F. Zhu, J. Wang, Y. Zhang, H. Tu, X. Xia, J. Zhang, H. He, H. Lin, M. Liu, Adv. Mater. 37 (2025) 2411601.
[38] J. Ding, T. Du, L.R. Jensen, S.S. Sørensen, D. Wang, S. Wang, L. Zhang, Y. Yue, M. M. Smedskjaer, Adv. Mater. 36 (2024) 2400652.
[39] R. Xu, A. Hu, Z. Wang, K. Chen, J. Chen, W. Xu, G. Wu, F. Li, J. Wang, J. Long, J. Energy Chem. 105 (2025) 35–43.
[40] X. Chu, F. Dong, Y. Jiang, Q. Qiao, H. Xie, J. Energy Chem. 105 (2025) 418–426.
[41] X. Cheng, W. Wang, Z. Tang, Y. Zhang, B. Chen, J. Zhang, F. Ye, J. Dong, H. Li, J. Jia, Q. Xiao, H. Lin, J. Wang, Angew. Chem. Int. Ed. (2026) e22417.
[42] J. Wang, J. Zhang, Y. Zhang, H. Li, P. Chen, C. You, M. Liu, H. Lin, S. Passerini, Adv. Mater. 36 (2024) e2402792.
[43] J. Wang, J. Zhang, J. Wu, M. Huang, L. Jia, L. Li, Y. Zhang, H. Hu, F. Liu, Q. Guan, M. Liu, H. Adenusi, H. Lin, S. Passerini, Adv. Mater. 35 (2023) e2302828.
[44] R. Xu, X.Q. Zhang, X.B. Cheng, H.J. Peng, C.Z. Zhao, C. Yan, J.Q. Huang, Adv. Funct. Mater. 28 (2018) 1705838.
[45] H. Zhang, X. Liao, Y. Guan, Y. Xiang, M. Li, W. Zhang, X. Zhu, H. Ming, L. Lu, J. Qiu, Y. Huang, G. Cao, Y. Yang, L. Mai, Y. Zhao, H. Zhang, Nat. Commun. 9 (2018) 3729.



Yongfeng Jia received his Ph.D. degree from Peking University in 2026. His research focuses on lithium-metal and aluminum-metal batteries, with particular interests in electrode/interface engineering and electrochemical reaction mechanisms.



Jinghai Liu is currently a professor and dean of the College of Chemistry and Materials at Inner Mongolia Minzu University, and director of the Inner Mongolia Key Laboratory of Nanocarbon Materials. His research interests focus on nanocarbon and inorganic solid materials for electrochemical energy storage, photocatalysis, and related functional applications. He has received several academic honors, including the Inner Mongolia Distinguished Young Scientists Fund and the Second Prize of the Inner Mongolia Natural Science Award.



Lei Ji is currently a research expert at the Peking University Ordos Energy Research Institute and previously conducted postdoctoral research at Tsinghua University. His research focuses on advanced energy-storage materials, particularly nanocarbon-based composites, interfacial electrocatalysis, and high-energy-density lithium–sulfur batteries, with emphasis on electronic-structure regulation and interfacial reaction mechanisms. He has published more than 20 SCI papers, including 10 as first or corresponding author, and has received several scientific awards, including the Second Prize of the Inner Mongolia Natural Science Award.



Dr. Jian Wang is a research fellow supported by Alexander von Humboldt foundation in Helmholtz Institute Ulm (HIU) and Karlsruhe Institute of Technology (KIT) after receiving his doctoral degree from University of Science and Technology of China. His research interests focus on the applications of catalysis in modulating electrochemical kinetics of secondary batteries (Catalysis-in-Batteries) and the exploration of in situ characterizations for probing interface mechanisms.